Geophysical Prospecting **EAGE** EUROPEAN ASSOCIATION OF GEOSCIENTISTS & ENGINEERS

ORIGINAL ARTICLE

Stochastic inversion of time-lapse electrical resistivity tomography data by means of an adaptive ensemble-based approach

Alessandro Vinciguerra[1,2,5] | **Mattia Aleardi**[1] | **Line Meldgaard Madsen**[3] |
Thue Sylvester Bording[4] | **Anders Vest Christiansen**[3] | **Eusebio Stucchi**[1]

[1]Earth Sciences Department, University of Pisa, Pisa, Italy

[2]Earth Sciences Department, University of Florence, Florence, Italy

[3]Department of Geoscience, Aarhus University, Aarhus, Denmark

[4]Aarhus GeoInstruments, Aarhus, Denmark

[5]CNRS, ENGEES, Institut Terre et Environnement de Strasbourg, UMR 7063, University of Strasbourg, Strasbourg, France

Correspondence
Alessandro Vinciguerra, Earth Sciences Department, University of Pisa, Via S. Maria 53, 56126 Pisa, Italy.
Email: alessandro.vinciguerra@unifi.it

Abstract

Inversion of time-lapse electrical resistivity tomography is an extension of the conventional electrical resistivity tomography inversion that aims to reconstruct resistivity variations in time. This method is widely used in monitoring subsurface processes such as groundwater evolution. The inverse problem is usually solved through deterministic algorithms, which usually guarantee a fast solution convergence. However, the electrical resistivity tomography inverse problem is ill-posed and non-linear, and it could exist more than one resistivity model that explains the observed data. This paper explores a Bayesian approach based on data assimilation, the ensemble smoother multiple data assimilation. In particular, we apply an adaptive approach in which the inflation coefficient is chosen based on the error function, that is the ensemble smoother multiple data assimilation restricted step. Our inversion approach aims to invert the data acquired at two different times simultaneously, estimating the resistivity model and its variation. In addition, the Bayesian approach allows for the assessment of the posterior probability density function needed for quantifying the uncertainties associated with the results. To test the method, we first apply the algorithm to synthetic data generated from realistic resistivity models; then, we invert field data from the Pillemark landfill monitoring station (Samsø, Denmark). Inversion results show that the ensemble smoother multiple data assimilation restricted step can correctly detect the resistivity variation both in the synthetic and in the field case, with an affordable computational burden. In addition, assessing the uncertainties allows us to interpret the reconstructed resistivity model correctly. This paper demonstrates the potential of the data assimilation approach in Bayesian time-lapse electrical resistivity tomography inversion.

KEYWORDS
time lapse, inversion, resistivity

INTRODUCTION

Electrical resistivity tomography (ERT) is a well-known active geophysical method widely practiced in near-surface geophysics, such as in groundwater exploration, landfill characterization and slope stability investigations (e.g. Chambers et al., 2009; Crawford et al., 2018; Hojat et al., 2019; Whiteley et al., 2017). This method is based on injecting an electric current into the ground through pairs of electrodes; the electric potential difference is recorded between other pairs of electrodes placed on the surface. The subsurface resistivity image is reconstructed by knowing the injected current level, the acquisition geometry and applying inversion algorithms. Nowadays, the development of multielectrode instruments and user-friendly inversion software has increased the feasibility of the method allowing its usage in different contexts (Batista-Rodríguez & Pérez-Flores, 2021; Gaël et al., 2017; Rubio-Melendi et al., 2018).

ERT is also increasingly becoming a common technique for monitoring purposes, for example in preventing water pollution from landfills (Audebert et al., 2014; Clément et al., 2011), assessing the levees' integrity (Arosio et al., 2017; Tresoldi et al., 2019) and inspecting the permafrost conditions (Hilbich et al., 2011). For Example, in recent years, autonomous systems for long-term permanent monitoring have been developed (Gunn et al., 2018; Tresoldi et al., 2019) for continuously tracking the subsurface resistivity variations.

A simple approach to obtaining information about subsurface resistivity evolution is acquiring data at different time steps. Then, inverting each time step independently and computing the difference between estimated resistivity models. However, this approach can only prevent artefacts from the result by employing heavy regularization techniques (Hayley et al., 2011). For this reason, more sophisticated time-lapse ERT (TL-ERT) inversion algorithms exist to mitigate these issues. Examples of TL algorithms are as follows:

- the cascade inversion that exploits a reference model as a starting point for inverting a second dataset (Miller et al., 2008);
- the difference inversion in which the difference between background and subsequent data is inverted (Labreque & Yang, 2001);
- inversion employing special mathematical norms such as L_p norm (Kim et al., 2013, Fiandaca et al., 2015).

All the mentioned deterministic algorithms are based on the iterative linearization of the error function around a current solution. The main advantage of this approach is that it requires a few forward calculations to converge towards the solution, resulting in a low computational burden. However, the result is a single model which usually explains the observed data without any uncertainty assessment. Theoretically, the uncertainties, in terms of posterior model covariance matrix, can be estimated from deterministic algorithms through the Hessian matrix, which defines the curvature of the error function in the vicinity of the current model (Liu et al., 2021). Specifically, Tarantola (2005) demonstrated that the posterior model covariance matrix can be approximated by the inverse of the linearized Hessian matrix. This strategy has been already followed by Auken et al. (2005) to retrieve at list a qualitative estimation of the uncertainties associated with the solution of 1D ERT inversion under the assumption of mildly non-linear problem.

However, as the topography of the error function obtained provides only a local information about the curvature of the error function, this approximation can hinder an accurate assessment of the model uncertainty (Fernández-Martínez et al., 2013).

In addition, the non-linearity and the ill-posedness can lead to an error function characterized by local minima and/or with a wide equivalence region of the solution. Consequently, depending on the starting model, deterministic algorithms can remain stuck in a local minimum or a minimum elongated valley, resulting in a misleading reconstructed resistivity model.

To overcome these issues, an alternative approach is to set the inverse problem in a probabilistic framework in which the posterior probability density function (pdf) associated with the model space is estimated. In this setting, the Markov Chain Monte Carlo algorithms (Mosegaard & Tarantola, 1995; Tarantola, 2005) approximate the posterior pdf through an iterative sampling but with an unfeasible computational time for large mode

l space dimensions. To reduce the computational workload maintaining the Bayesian framework, we should reduce the dimension of parameter space (e.g. Aleardi et al., 2021a; Grana et al., 2019; Vinciguerra et al., 2021). In this work, we follow a different strategy that employs an ensemble-based data-assimilation method, which guarantees uncertainty assessment with a moderate number of forward calculations (Aleardi et al., 2021b). The data-assimilation approach was initially proposed in the context of ocean dynamics (Evensen, 1994) and, more recently, in petroleum engineering for reservoir characterization (Chen & Oliver, 2013; Le et al., 2016). In the ensemble-based method, the ensemble kalman filter and the ensemble smoother (ES) are the most popular (Emerick & Reynolds, 2013). The first method sequentially assimilates data in time, whereas the ES assimilates all the data available to update the ensemble globally. It can be demonstrated that a single data assimilation step of the ES algorithm is equivalent to a single Gauss–Newton one with sensitivity assessed from the ensemble (Reynolds et al., 2006). In 2012, Emerick and Reynolds introduced the multiple data assimilation methods (MDA), which were integrated with ES to give the ES-MDA. In this way, the MDAs'

steps correspond to sequential small Gauss–Newton corrections, which ease the convergence, especially in the case of the non-linear problem. In this paper, we apply an adaptive ES-MDA algorithm, the ES-MDA restricted step (ES-MDA-RS, Le et al., 2016), that adapts the inflation coefficient across the iterations. In particular, this approach allows computing the inflation coefficient according to the error function automatically.

The aim is to limit the effect of overshooting issues, which occur when the data predicted from the initial guess are far from the observed one, thus resulting in a large data mismatch. The final model will present unrealistic high and/or low value of some model parameters (Gao & Reynolds, 2006; Li et al., 2003). In that context, we implement the ES-MDA-RS algorithm for the TL-ERT simultaneous inversion. We invert two datasets together for simultaneous inversion to assess the reference model and its resistivity variation. In this work, we employ finite elements forward modelling extracted from the BERT software package (Gunther & Rucker, 2012) to calculate the predicted data from the subsurface resistivity. We first apply the ES-MDA-RS to invert apparent resistivity data simulated by building two synthetic models to test the approach. Then, we inverted field data from the Pillemark landfill monitoring station (Samsø, Denmark) to identify near-surface resistivity variation and the associated uncertainties. Finally, we compare the result of the field inversion with the deterministic TL algorithm.

METHODS

The Bayesian inversion aims to estimate the posterior probability density function (pdf) of the model knowing the data and some prior knowledge of the model parameters. In this work, we define the model as the subsurface resistivity $\boldsymbol{\rho}$, whereas the data as the observed apparent resistivity $\boldsymbol{\rho}_a$.

Assuming that we know the prior distribution of the model parameters $p(\boldsymbol{\rho})$ and the data-likelihood distribution $p(\boldsymbol{\rho}_a|\boldsymbol{\rho})$, the data-assimilation problem can be formulated through the Bayes theorem (Evensen et al., 2022):

$$p\left(\boldsymbol{\rho}|\boldsymbol{\rho}_a\right) = \frac{p(\boldsymbol{\rho})\, p(\boldsymbol{\rho}_a|\boldsymbol{\rho})}{p\left(\boldsymbol{\rho}_a\right)}, \qquad (1)$$

where $p(\boldsymbol{\rho}_a)$ is the marginal pdf of the observed data that is usually a normalizing coefficient that makes the integral of the posterior pdf equal to 1 over the entire model space. In this context, the $p(\boldsymbol{\rho}|\boldsymbol{\rho}_a)$ is the solution of the data-assimilation problem. The Bayes theorem shows that the pdf is equal to the product between prior and likelihood distribution. However, for non-linear forward operators, the target $p(\boldsymbol{\rho}|\boldsymbol{\rho}_a)$ can be only numerically evaluated, for example one method that can be used is the data-assimilation technique.

We implement the ensemble smoother (ES) multiple data assimilation (MDA) with restricted step (ES-MDA-RS, Le et al., 2016) an adaptive version of the ES-MDA algorithm (Emerick et al., 2013, Aleardi et al., 2021; Grana et al., 2019) that we modified for time-lapse (TL) purposes. Under the assumptions of Gaussian distributed model parameters and data noise, the algorithm starts with an ensemble of models drawn from the prior distribution in which we impose spatial continuity through a Gaussian variogram. The ES-MDA-RS performs iterative Bayesian updating of the current ensemble of models through multiple assimilation steps (iterations). At the end of the entire procedure, the posterior pdf can be numerically estimated from the ensemble of models at the last iteration. The updating equation is defined as follows:

$$\boldsymbol{\rho}_i^{k+1} = \boldsymbol{\rho}_i^k + \mathbf{K}\left(\boldsymbol{\rho}_a + \mathbf{r}_i^k - f(\boldsymbol{\rho}_i^k)\right), \qquad (2)$$

with $i = 1, \ldots, N_e$ with N_e the number of the ensemble members, k is the index of the assimilation step, $\boldsymbol{\rho}_i^{k+1}$ is the updated resistivity model, $\boldsymbol{\rho}_i^k$ is the resistivity model at the previous iteration, $\boldsymbol{\rho}_{a i}$ is the observed apparent resistivity data vector perturbated through a random vector $\mathbf{r}_i^k$ drawn from $\sqrt{\alpha_k \mathbf{C}_{\rho a}} N(0, \mathbf{I})$, where $\mathbf{C}_{\rho_a}$ is the data covariance, α is the inflation coefficient, and f is the forward operator. The $\mathbf{K}$ represents the Kalman gain filter which is expressed by

$$\mathbf{K} = \mathbf{C}_{\rho\rho_a}\left(\mathbf{C}_{\rho_a\rho_a} + \alpha\mathbf{C}_{\rho_a}\right)^{-1}, \qquad (3)$$

where $\mathbf{C}_{\rho\rho_a}$ is the cross-covariance matrix between models and predicted data, $\mathbf{C}_{\rho_a\rho_a}$ is the covariance matrix of the data predicted by the ensemble of models, and $\mathbf{C}_{\rho_a}$ denotes the covariance of the observed data. Different types of noises and errors can affect the dataset, and their correct characterization can improve the imaging of the subsurface (Tso et al., 2017). For instance, Ramirez et al. (2005) stated that the multi electrodes system can increase the probability that the data errors are correlated. Moreover, the forward modelling error can introduce uncorrelated and correlated errors that should be taken into the account. However, the adopted inversion algorithm assumes Gaussian distribution of the errors (Evensen et al., 2022), and for simplicity, we assume uncorrelated noise and negligible errors generated by the forward modelling.

In this work, we apply the adaptive ES-MDA-RS (Le et al., 2016) in which α factor varies across the iterations. In particular, it has been suggested (Oliver et al., 2008, Emerick & Reynolds, 2013; Le et al., 2016; Emerick, 2019) that setting a large initial inflation factor and decreasing it during the assimilation steps can provide better results. The meaning is that at the first iterations, the difference between observed and predicted data is large, and it could result in an overcorrection of the current model. Thus, we can consider the inflation

coefficient as a sort of damping factor which reduces the model updating.

Defining the average (E_M) and normalized error function $(\bar{E}_M)$ as (Le et al., 2016)

$$\bar{E}_M = \frac{1}{N_e} \sum_{i=1}^{N_e} E_{M,i}, \qquad (4)$$

$$E_M = \frac{1}{2M} \sum_{i=1}^{N_e} \left(f\left(\boldsymbol{\rho}_i\right) - \boldsymbol{\rho}_a\right)^T \mathbf{C}_{\rho_a}^{-1} \left(f\left(\boldsymbol{\rho}_i\right) - \boldsymbol{\rho}_a\right), \qquad (5)$$

where M is the size of data vector, N_e the dimension of the ensemble, i is the index of the ith ensemble member, and the inflation factor is set as $\alpha_k = 0.25 \times \bar{E}_M$ (Le et al., 2016).

The algorithm steps of ES-MDA-RS are the following:

1. Generate the ensembles of prior realizations and for each kth assimilation step.
2. Compute the predicted data for each ensemble member through the forward operator f.
3. Calculate the average normalized error function $\bar{E}_M$, Equations (4) and (5).
4. Perturb the observed data through the relation $\tilde{\boldsymbol{\rho}}_a = \boldsymbol{\rho}_a + \sqrt{\alpha_k} \mathbf{C}_{\rho_a}^{\frac{1}{2}} \mathbf{n}$, with $\mathbf{n} = N(0, \mathbf{I})$ and $\alpha_k = 0.25 \times \bar{E}_M$.
5. Update the ensemble with Equations (2) and (3).
   - If the average updating is higher than two times the prior standard deviation, the α_k is doubled and steps 3 and 4 are repeated.
6. Calculate the sum of the inverse of the inflation coefficient up to the current iteration:

$$\gamma = \sum_{k=1}^{N} \frac{1}{\alpha_k}, \qquad (6)$$

   - if $\gamma = 1.0$ the algorithm stops;
   - if $\gamma < 1.0$ the algorithm continues;
   - if $\gamma > 1.0$ the algorithm repeats steps 3–4 and adjusts α_k to fulfil the condition $\gamma = 1$.

In the common ES-MDA algorithm, α_k is selected such that $\sum_{k=1}^{Nit} \frac{1}{\alpha_k} = 1$ and for simplicity, it is kept constant at each iteration (Aleardi et al., 2021). Due to the analogy between ES and the Gauss–Newton approach (Reynolds et al., 2006), the role of the inflation coefficient can be seen as a regularizing factor that prevents the overshooting issue which may happen at the first iteration steps (Reynolds et al., 2006). Theoretically, from step 3 of the algorithm, we expect a decrease of the regularization factor during the assimilation process that should improve the quality of the estimated models (Emerick & Reynolds, 2013).

To correctly assess the posterior pdf, the ensemble dimension N_e must be large enough to avoid an underestimation of

the model uncertainty and small enough to maintain a reasonable computational cost. At the end of the minimization, the outcome is an ensemble of posterior realization which approximates the posterior pdf and from which we can compute the uncertainties associated with each cell of the model.

From the TL point of view, the goal is to map the resistivity variation in time. The simplest approach is to perform two separate inversions and then compute the difference between the estimated models. However, this strategy produces an amplification of the inversion artefacts (Kim et al., 2009). For these purposes, we apply a simultaneous inversion in which the resistivity models at two-time instants (t_0 and t_1), and the corresponding uncertainties are evaluated in a single inversion run. We define the total apparent resistivity vector $\boldsymbol{\rho}_a$ as

$$\boldsymbol{\rho}_a = \begin{bmatrix} \boldsymbol{\rho}_{a0} \\ \boldsymbol{\rho}_{a1} \end{bmatrix} = \begin{bmatrix} f\left(\boldsymbol{\rho}_0\right) \\ f\left(\boldsymbol{\rho}_1\right) \end{bmatrix} = \begin{bmatrix} f\left(\boldsymbol{\rho}_0\right) \\ f\left(\boldsymbol{\rho}_0 \cdot \boldsymbol{\lambda}_\rho\right) \end{bmatrix}, \qquad (7)$$

where $\boldsymbol{\rho}_{a0}$ is the apparent resistivity vector observed at t_0, $\boldsymbol{\rho}_{a1}$ is the apparent resistivity vector at the time t_1, and $\boldsymbol{\lambda}_\rho = \boldsymbol{\rho}_1/\boldsymbol{\rho}_0$ is the resistivity variation defined as the ratio between the subsurface resistivity at the second time step $\boldsymbol{\rho}_1$, and at the first-time step $\boldsymbol{\rho}_0$. Consequently, we expect the following range of variations:

$$\boldsymbol{\lambda}_\rho = \boldsymbol{\rho}_1/\boldsymbol{\rho}_0 = \begin{cases} > 1 & \text{if } \boldsymbol{\rho}_0 < \boldsymbol{\rho}_1 \text{ positive variation} \\ 1 & \text{if } \boldsymbol{\rho}_0 = \boldsymbol{\rho}_1 \quad \text{no variation} \\ < 1 & \text{if } \boldsymbol{\rho}_0 > \boldsymbol{\rho}_1 \text{ negative variation} \end{cases}. \qquad (8)$$

In the TL context, we can rewrite updated Equation (2) as

$$\bar{\boldsymbol{\rho}}_i^{k+1} = \bar{\boldsymbol{\rho}}_i^k + \mathbf{K}\left(\bar{\boldsymbol{\rho}}_a + \mathbf{r}_i^k - f\left(\bar{\boldsymbol{\rho}}_i^k\right)\right), \qquad (9)$$

where $\bar{\boldsymbol{\rho}}_i^k$ is the total resistivity vector containing both $\boldsymbol{\rho}_0$ and $\boldsymbol{\lambda}_\rho$, and $\bar{\boldsymbol{\rho}}_a$ is the total apparent resistivity vector composed by $\boldsymbol{\rho}_{a0}$ and $\boldsymbol{\rho}_{a1}$. The covariance matrices of the Kalman Gain Filter, Equation (3), become

$$\mathbf{C}_{\rho \rho_a} = \begin{bmatrix} \mathbf{C}_{\rho_0 \rho_{a0}} & 0 \\ 0 & \mathbf{C}_{\lambda_\rho \rho_{a1}} \end{bmatrix}, \qquad (10)$$

$$\mathbf{C}_{\rho_a} = \begin{bmatrix} \mathbf{C}_{\rho_{a0}} & 0 \\ 0 & \mathbf{C}_{\rho_{a1}} \end{bmatrix}, \qquad (11)$$

$$\mathbf{C}_{\rho_a \rho_a} = \begin{bmatrix} \mathbf{C}_{\rho_{a0} \rho_{a0}} & 0 \\ 0 & \mathbf{C}_{\rho_{a1} \rho_{a1}} \end{bmatrix}. \qquad (12)$$

In Equation (10), $\mathbf{C}_{\rho_0 \rho_{a0}}$ represents the cross-covariance between the model ensemble of resistivity model (P) and
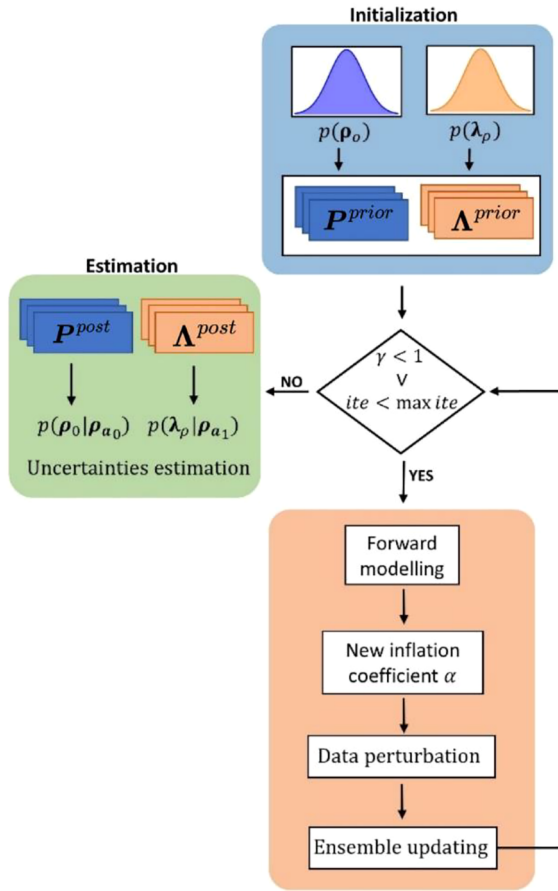
Geophysical Prospecting

FIGURE 1 Flow chart of the ensemble smoother (ES-)multiple data assimilation (MDA)-restricted step (RS) algorithm. *ite* represents the current iteration, max *ite* the maximum number of iterations allowed, P^{prior} and Λ^{prior} are the two ensembles of prior realizations and P^{post} and Λ^{post} the two ensembles of posterior realizations.

FIGURE 2 (a) Resistivity model ρ_0 at the simulated acquisition time t_0. (b) Resistivity model ρ_1 at the second time t_1. (c) Resistivity variation in terms of the ratio between ρ_1 and ρ_0.

the data ensemble of the first-time step; $\mathbf{C}_{\lambda_\rho \rho_{a1}}$ the cross-covariance between the ensemble of variation (Λ) of resistivity and the ensemble of data of the second time step.

In Equation (11), $\mathbf{C}_{\rho_{a0}}$ and $\mathbf{C}_{\rho_{a1}}$ are diagonal matrices containing the covariance of the data ρ_{a0} and ρ_{a1}, respectively.

In Equation (12), $\mathbf{C}_{\rho_{a0}\rho_{a0}}$ is the covariance matrix of the ensemble of predicted data at the time-step t_0, whereas $\mathbf{C}_{\rho_{a1}\rho_{a1}}$ is the covariance matrix of the ensemble of predicted data at the time-step t_1.

Evensen et al. (2022) explained the link between ES- MDA and Gauss–Newton algorithm. The cross-covariance matrix $\mathbf{C}_{\rho\rho_a}$ and the matrix $\mathbf{C}_{\rho_a\rho_a}$ in Equations (10) and (12) contain information about the sensitivity of the forward operator. In particular, the two matrices approximate the following relations (Reynolds et al., 2006):

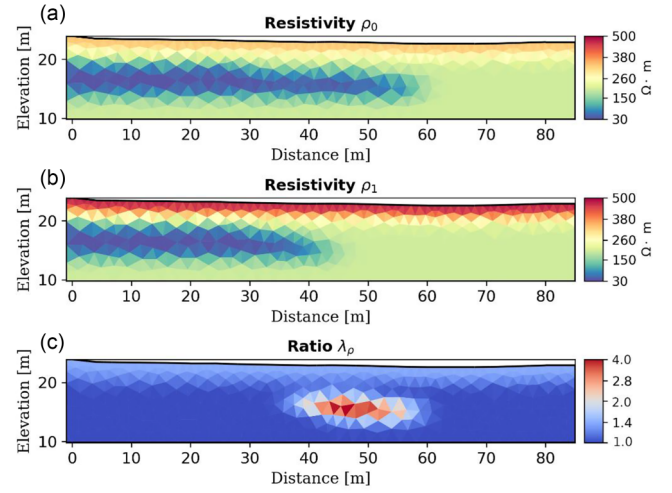$$\mathbf{C}_{\rho\rho_a} \approx \mathbf{C}_m \mathbf{H}^T, \tag{13}$$

$$\mathbf{C}_{\rho_a\rho_a} \approx \mathbf{H}\mathbf{C}_m\mathbf{H}^T, \tag{14}$$

$$\mathbf{H} = \nabla_m f(\bar{m}), \tag{15}$$

where $\mathbf{H}$ is the sensitivity kernel defined as the sensitivity of the predicted data computed on the mean model $\bar{m}$ and $\mathbf{C}_m$ is the covariance matrix of the model parameters. Note that the matrices are calculated from the entire ensemble of current models. In other words, the sensitivity information carried out by the covariance and cross-covariance matrices are computed considering the entire ensemble of models.

The merging between the ES-MDA-RS and the described TL approach allows to invert simultaneously the resistivity ρ_0 and its variation λ_ρ; the flow chart of the algorithm is shown in Figure 1.

From the ensembles of posterior realizations, we can quantify the uncertainties associated with the estimated model by computing the standard deviation of each marginal distribution. An alternative to interpret the uncertainty is the coefficient of variation (cv) which is widely used in different fields, and it is a measure of the variability in relation to the mean (Everitt, 1998). It is computed by normalizing the standard deviations by the mean value of each resistivity cell to avoid misleading interpretations affected by large range of resistivity values. Thus, the cv is defined as follows (Liu, 2012):
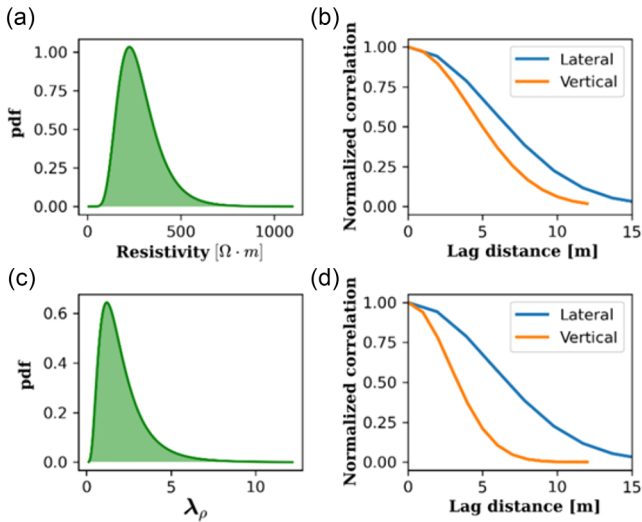
$$cv_i = \frac{\sigma_i}{\mu_i}, \tag{16}$$

FIGURE 3 (a) Prior marginal distribution associated with each cell of ρ_0. (b) Spatial correlation associated with the 2D Gaussian variogram and assumed for ρ_0; the lateral and the vertical correlations are represented in blue and orange, respectively. (c) Prior marginal distribution associated with each cell of λ_ρ. (d) Spatial correlation associated with the 2D Gaussian variogram and assumed for λ_ρ.

TABLE 1 Parameters of prior distributions and Gaussian variograms (note that the mean and the standard deviations are expressed in logarithmic domain).

	Prior mean	Prior std	α_x	α_y
ρ_0	5.41	0.38	8	6
λ_ρ	0.18	0.6	8	4

by Miller et al. (2008), a deterministic strategy that employs the estimated model at t_0 as the starting point for inverting the data at t_1. This approach properly reconstructs the subsurface resistivity cells that are well-illuminated by the data, whereas the other values should remain equal to the reference model (Hayley et al., 2011). To perform the cascade inversion, we exploit the BERT software package (Gunther & Rucker, 2012).

SYNTHETIC TESTS

To check the effectiveness of the ensemble smoother (ES)-multiple data assimilation (MDA) restricted step (ES-MDA-RS) for time-lapse (TL) inversion, we decide to build a simple resistivity model that simulates an advancing low resistivity plume and a seasonal shallow resistivity variation. Specifically, we create a plume of 30 Ω m reproducing a water flow within a homogeneous background of 200 Ω m and a shallow layer of 300 Ω m (Figure 2a). To build the variation, we mimic a regression of a water or contaminant plume from the first acquisition time t_0 and the second one t_1, and we
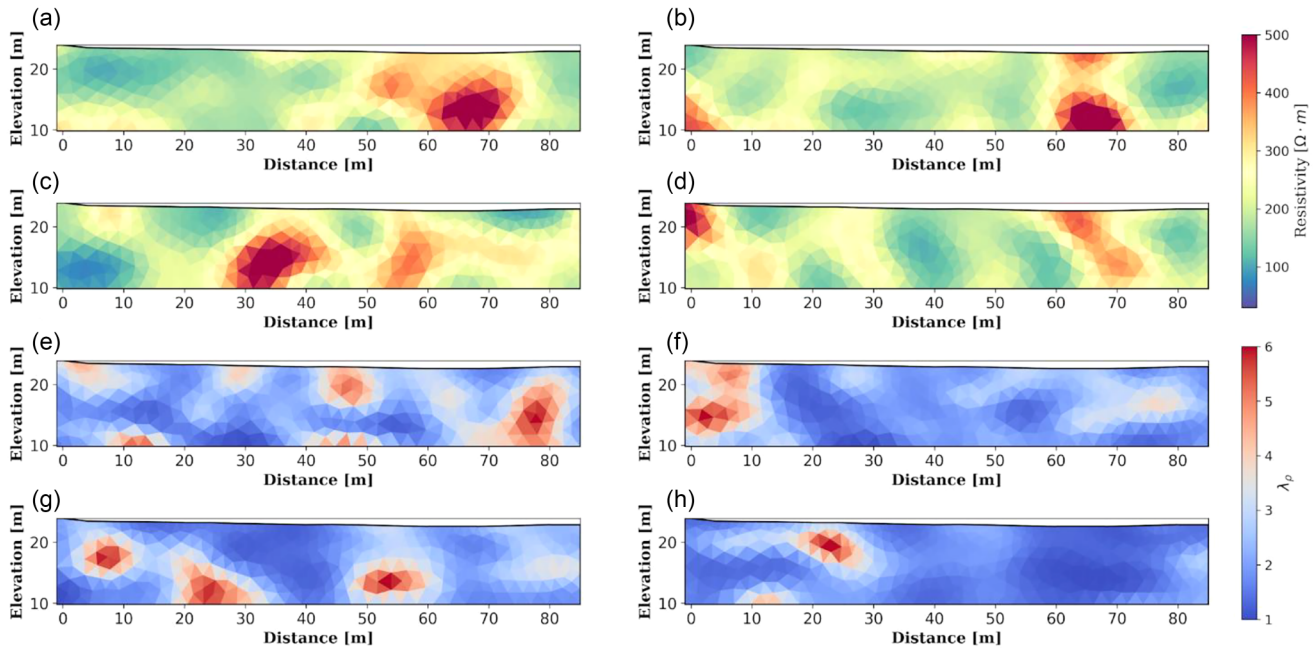
where i is the index of the model cell. Usually, the cv is multiplied by 100 obtaining the percentage of variation. This relation allows an easier interpretation of the posterior uncertainties by expressing the dispersion of the resistivity value around the mean.

To compare the results of the ES-MDA-RS inversion algorithm, we employ the cascaded inversion approach described

FIGURE 4 (a–d) Realizations drawn from the prior ensemble P^{prior}. (e–h) Realizations drawn from the ensemble Λ^{prior}.

also simulate an increase of resistivity of the shallow layer from 300 to 500 Ω m (Figure 2b). The resulting variation, defined as the ratio between $\boldsymbol{\rho}_1$ and $\boldsymbol{\rho}_0$, is represented in Figure 2c.

The goal of the TL synthetic test is to reconstruct the resistivity changes that we impose at a distance between about 40 and 60 m and the shallow one. After generating the synthetic data, the first step is to define the two probability density function which should contain our prior knowledge about the model $\boldsymbol{\rho}_0$ and the variation $\boldsymbol{\lambda}_\rho$. We calculate the mean and the standard deviation of the prior model from the first synthetic data $\boldsymbol{\rho}_{a0}$ and from the ratio between $\boldsymbol{\rho}_{a1}$ and $\boldsymbol{\rho}_{a0}$. The marginal prior distributions are shown in Figure 3a,c. In addition, we define a Gaussian variogram to add a spatial correlation between the model parameters. Considering the vertical direction y, the correlation is expressed by

$$\boldsymbol{\tau}_y = \exp\left(-\frac{h_y^2}{a_y^2}\right), \qquad (17)$$

where h_y is the distance of the spatial correlation function along the y direction, and a_y is the effective range of the variogram along the same direction. In this test, we set a_x equal to 8 m and a_y equal to 6 m for $\boldsymbol{\rho}_0$ and a_x equal to 8 m and a_y equal to 4 m for $\boldsymbol{\lambda}_\rho$ (Figure 3b–d, Table 1). Practically, this choice can be inferred from previous information about the subsurface. In this case, the correlation guarantees a higher lateral than vertical continuity of the resistivity anomalies (Figure 4). After defining the marginal prior distributions and the model covariance, we draw two ensembles of 2000 prior realizations (P^{prior} and Λ^{prior} associated with $\boldsymbol{\rho}_0$ and the $\boldsymbol{\lambda}_\rho$, respectively). Figure 4 shows examples of four prior realizations drawn from each ensemble; note that the prior realizations contain resistivity values that are constrained by the prior distributions in Figure 3a,c and the imposed spatial correlation pattern.

We generated the observed data using a combination of multiple gradient array and dipole–dipole composed of 406 quadrupoles on 22 electrodes with 4 m spacing. Without a quantitative study of the statistics of the noise affected the TL dataset, and under the assumption of Gaussian error required by the data assimilation algorithm, we contaminate the data with uncorrelated Gaussian noise with standard deviation equal to 2% of the apparent resistivity values.

To solve the 2.5D forward problem, we exploit the BERT software package that employs a finite elements discretization (Gunther & Rucker, 2012). As expected, the calculated synthetic pseudo sections (Figure 5) show an apparent resistivity decrease at the shallow pseudo depth and at the left side of the pseudo section.

We use the ES-MDA-RS algorithm to automatically stop the inversion process after the maximum iteration number; in this synthetic test, we set the maximum iteration number
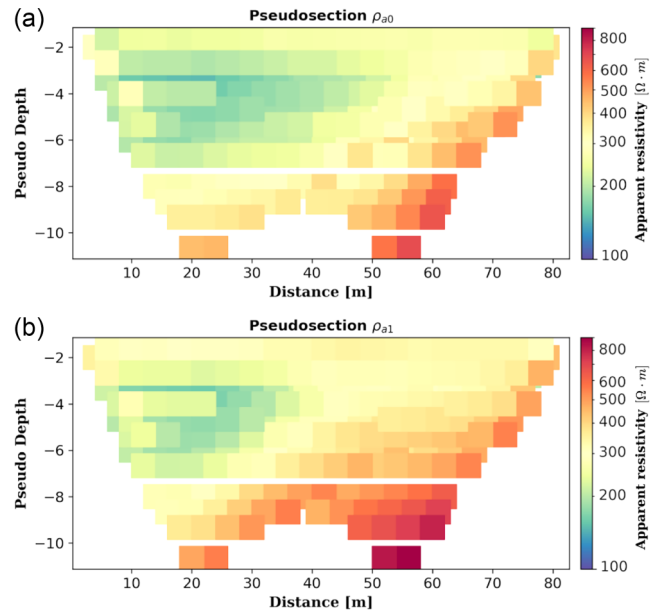

FIGURE 5 (a) Synthetic pseudo section representing the resistivity data at the time zero t_0, ρ_{a0}. (b) Synthetic pseudo section representing the resistivity data at the time t_1, ρ_{a1}.

equal to 5. The inversion takes approximately 85 min to run on an Intel Xenon CPU E5-2420 v2 @ 2.20 GHz, and the computational cost is about 85 min. The algorithm returns two ensembles of models, P^{post} and Λ^{post}, approximating the posterior distributions $p(\boldsymbol{\rho}_0|\boldsymbol{\rho}_{a0})$ and $p(\boldsymbol{\lambda}_\rho|\boldsymbol{\rho}_{a1})$ from which we compute the mean models and the uncertainty (see Figure 1). The cross-plot and the root mean square error (RMSE) suggest that the means of the ensembles; are able to predict the data satisfactorily (Figure 6a,b). In particular, the RMSE is 0.62% for $\boldsymbol{\rho}_{a0}$ and 0.69% for $\boldsymbol{\rho}_{a1}$ and it constantly decreases across the iterations (Figure 6c). The inflation coefficient, which we define as a function of the error function according to Equation (4), is represented in Figure 6d. We observe that it abruptly decreases from iteration 0 to 1 and it continues to decrease until the last iteration.

The mean models of the ensembles P^{post} and Λ^{post} are represented in Figure 7d–f in comparison with the synthetic true models (Figure 7a–c). The mean model $\boldsymbol{\rho}_0$ (Figure 7d) suggests that the algorithm is able to well reconstruct the shallow high resistivity layer and the low resistivity plume as well. Moreover, the shallow resistivity variation and the central large one (caused by the regressing plume) are recovered with a good spatial resolution (Figure 7e). The resulting resistivity model at the time t_1, estimated through Equation (8), is represented in Figure 7f. It exhibits an increment of resistivity of the shallow layer, and good reconstruction of the regressing plume. The estimated mean models exhibit few artefacts that do not compromise the data fitting quality. We observe that they are mainly located at the bottom and at the edge of the model where we expect poor data illumination.

The evaluation of the uncertainty is performed computing the standard deviation cell by cell from the ensembles P^{post} and Λ^{post}. However, we also evaluate the uncertainties computing the coefficient of variation (cv% (Equation 16), which can be viewed as a normalized standard deviation for the mean value. The standard deviation in Figure 8b indicates that the left bottom and bottom right edge resistivity are not reliable due to high uncertainty values. Moreover, the cv (Figure 8c) confirms the model ambiguity at the bottom and lateral edges of the study area. The quantification of uncertainties helps us to interpret the TL resistivity variation in Figure 8d. In par-

ticular, high values of standard deviation are located at the bottom left and right but also in correspondence with the central well-predicted resistivity variation (Figure 8e). However, the coefficients of variation in Figure 8f exhibit that the variability of the resistivity values is relevant only at the bottom and at the lateral edges (cv of about 25%), similar to Figure 8c. This similarity can be motivated by the fact that, being a TL inversion, the survey configuration is maintained the same between the acquisition steps; therefore, assuming that the resistivity of the subsurface is not dramatically changed the sensitivity patter is similar.
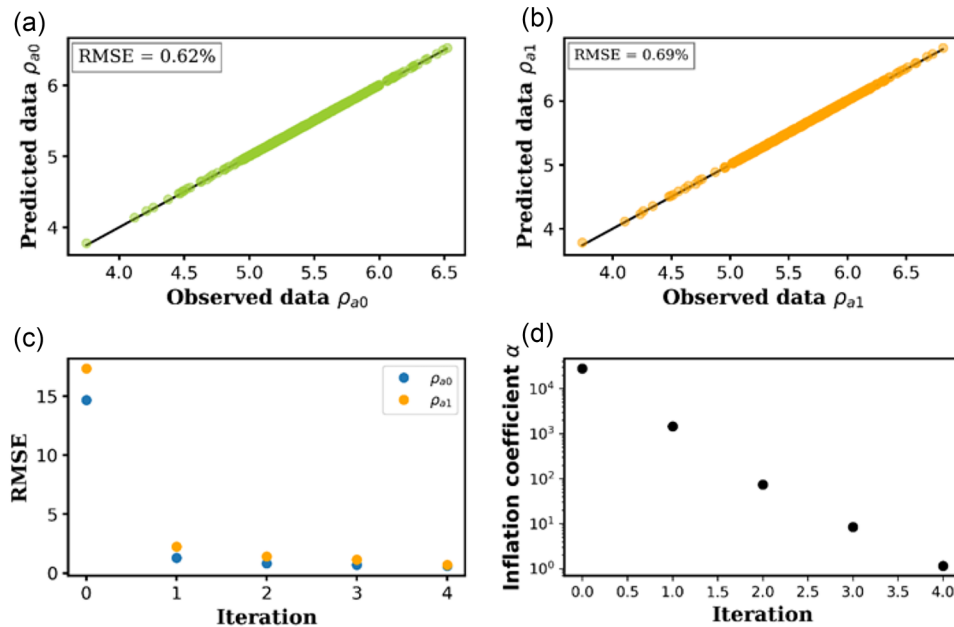
FIGURE 6 (a) Data misfit and apparent resistivity ρ_{a0} cross-plot. (b) Data misfit and apparent resistivity ρ_{a1} cross-plot. (c) Evolution of root mean square error (RMSE) during the iterations. (d) Inflation factors values of each iteration.
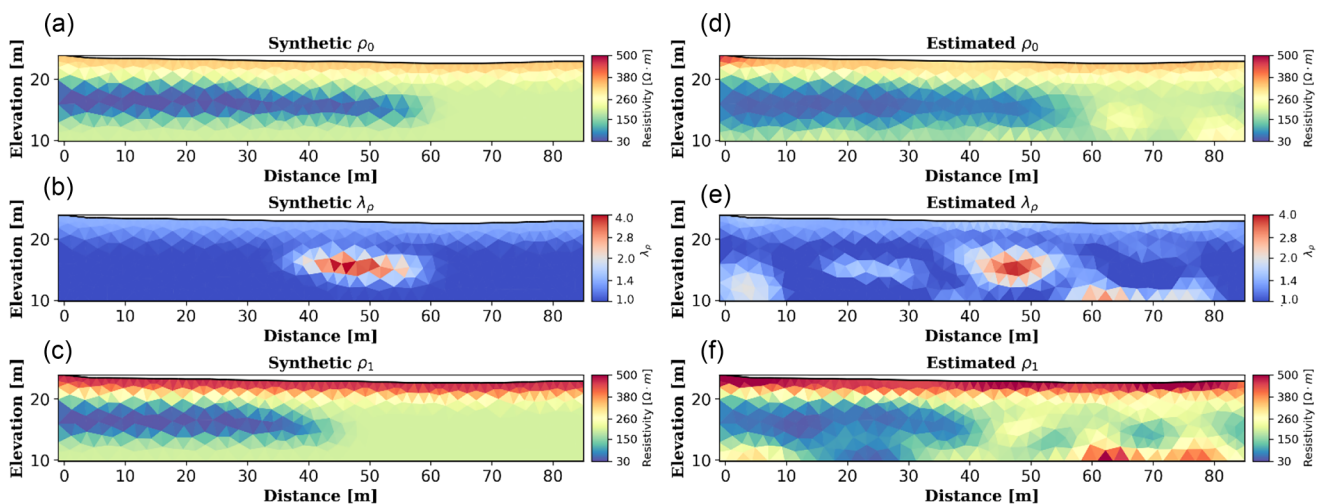

FIGURE 7 (a–c) Synthetic reference model. (d) Predicted mean model ρ_0. (e) Predicted mean variation of resistivity λ_ρ. (f) Predicted model ρ_1 computed as the product between ρ_0 and λ_ρ.

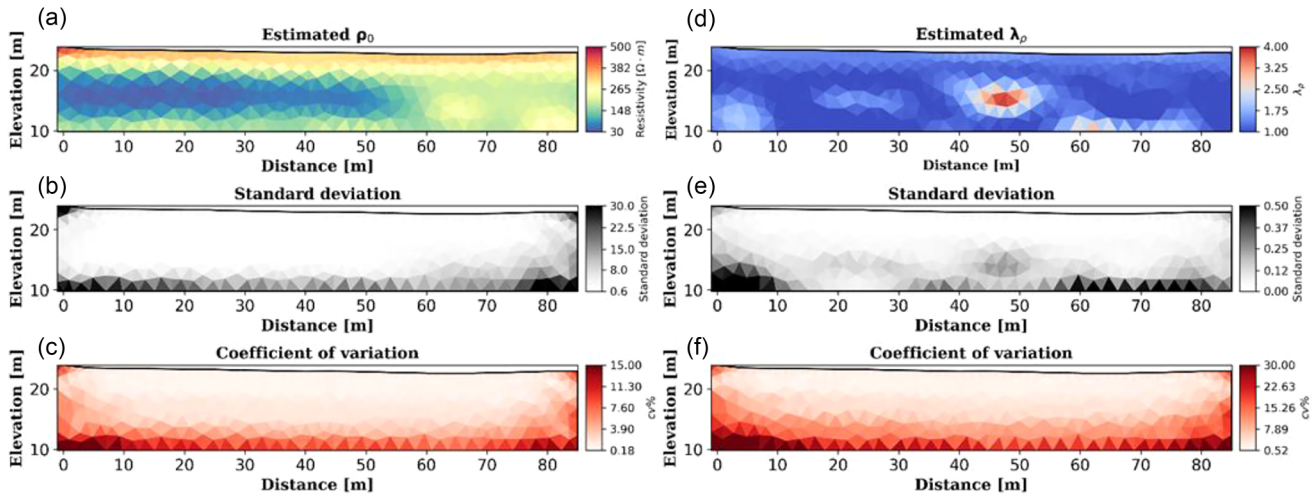**Geophysical Prospecting**

FIGURE 8 (a) Mean ensemble model ρ_0. (b) Uncertainties associated with ρ_0. (c) Coefficients of variation associated with ρ_0. (d) Mean ensemble variation λ_ρ. (e) Standard deviation associated with ρ_1. (f) Coefficients of variation associated with λ_ρ.
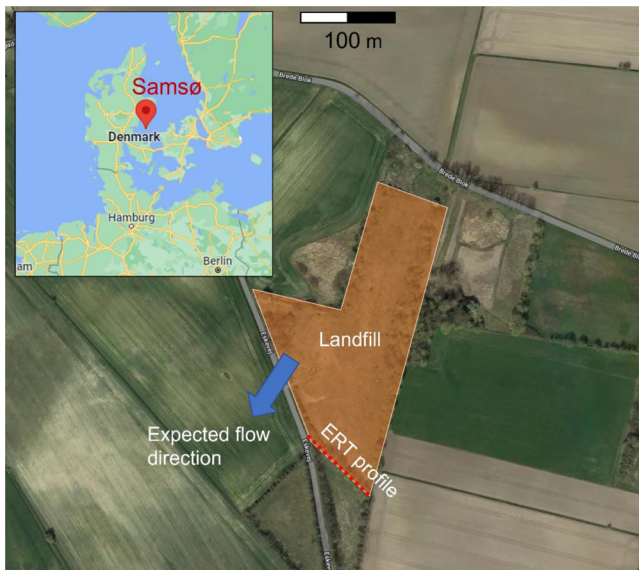

FIGURE 9 Aerial view of the Pillemark landfill, the electrical resistivity tomography (ERT) profile is indicated by the red dots.

FIELD DATA INVERSION

We now discuss the inversion of 2D data acquired by the Pillemark landfill monitoring station in Samsø island (Denmark) (Figure 9).

The goal of the monitoring project was to assess the pollution risk of the aquifers supervising the groundwater evolution through the integration of electrical resistivity tomography (ERT) ad IP datasets (Bording et al., 2018). However, in this work, we focus on the direct current measurements only. The geology of the site is composed of a fill cover over a sand layer of various grain sizes and moraine clays that underlies the sand layer. We aim to invert two datasets acquired 1 year
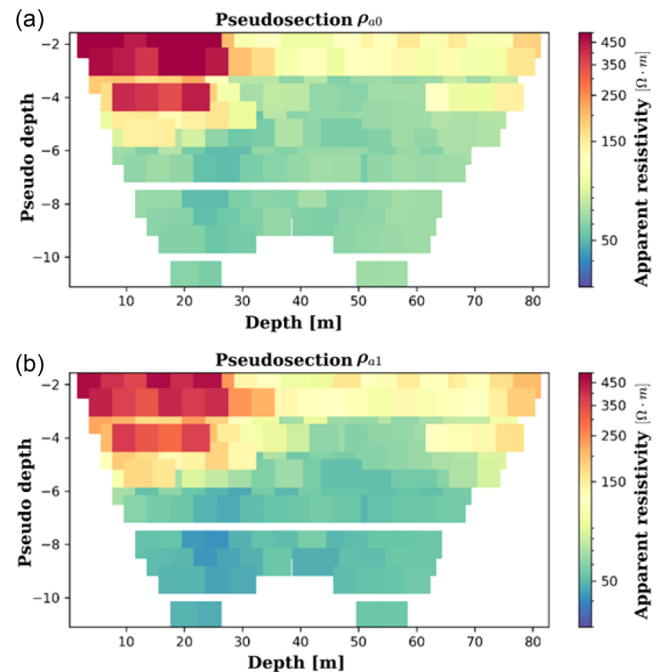
FIGURE 10 (a) Observed data on 27th March 2016. (b) Observed data on 28th March 2017.

apart, 27 March 2016 and 28 March 2017, respectively. This choice is made to limit the shallow seasonal effects that could affect the datasets. After removing outliers and negative resistivity values, the number of data points for each dataset is 336; Figure 10 shows the two pseudo sections.

We start building two ensemble, P^{prior} and Λ^{prior}, each drawn from two Gaussian distributions and according to the assumed Gaussian variograms (Figure 11a,c). The moments of the distributions are computed from the observed data, paying attention to avoid underestimation of the standard
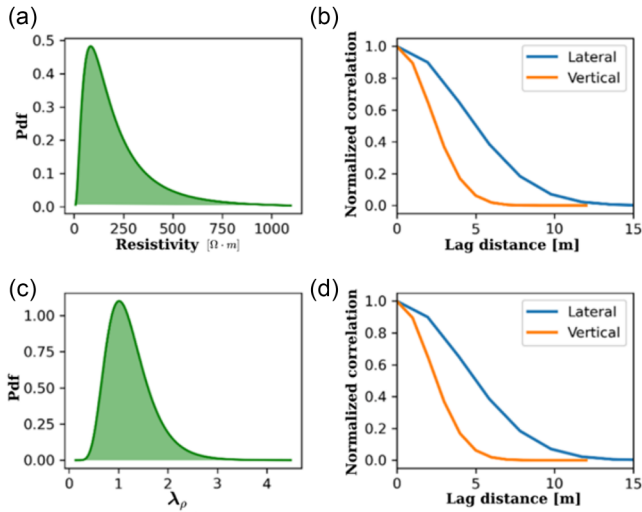
FIGURE 11 (a) Prior marginal log-Gaussian associated with each cell of the model ρ_0. (b) Spatial correlation associated with the 2D Gaussian variogram and assumed for ρ_0. (c) Prior marginal log-Gaussian distribution associated with each cell of the model λ_ρ. (d) Spatial correlation associated with the 2D Gaussian variogram and assumed for λ_ρ.

deviation. As from previous investigations (Bording et al., 2018) and geological information (Høyer et al., 2019), we expect a mainly horizontal deposits and impose a lateral correlation range (a_x) of 6 m and a vertical correlation (a_y) of 4 m both for the resistivity model and the resistivity change (Figure 12b–d). The choice of the ensemble dimension has been evaluated repeating the inversion and changing the ensemble member; Figure 12 shows the results in terms of root mean square error (RMSE) % and estimated uncertainty employing 500, 2000, 3000 and 30,000 models. Even though the prediction error is not heavily affected by the ensemble size (Figure 12a,b), the uncertainty can be underestimated if a proper number size is not considered. For instance, the coefficients of variation associated with the model ρ_0 in Figure 12c (500 models) seem to be underestimated in comparison with Figure 12d (2000 models). On the other hand, the uncertainty assessed through ensembles of size 2000, 3000 and 30,000 models is comparable and shows coefficients of variation up to 50% in depth and laterally. Therefore, considering the computational cost, we decide to employ two ensembles of 2000 models. Figure 13a–d shows six realizations drawn from the ensemble P^{prior}, whereas Figure 13e–h shows six realizations drawn from the ensemble Λ^{prior}.

Table 2 summarizes the selected parameters for the inversion. After setting the maximum iteration number, the inversion process ends if the summation of Equation (6) is equal to 1 or if the maximum number of iterations is reached. In this inversion, we set the maximum number of iterations equal to 10, but the inversion stops at the 7th iteration after 109 min on an Intel Core i7-8700 CPU @ 3.20 GHz personal com-

TABLE 2 Parameters of prior distributions and Gaussian variograms (note that the mean and the standard deviations are expressed in logarithmic domain).

	Prior mean	Prior std	α_x	α_y
ρ_0	4.3	0.7	6	3
λ_ρ	0.004	0.05	6	3

puter. As in the synthetic test, the data fitting is quantified through the cross-plot and RMSE between observed and predicted data. Figure 14a,b exhibits an RMSE of 3.1% for the prediction ρ_{a0} and an RMSE of 3.7% for the prediction of ρ_{a1}, which demonstrates a satisfying result in terms of data fitting. The mean models computed from the ensembles at each iteration allow to evaluate the prediction error during the entire inversion process. We observe that the error decreases from the first to the last iteration, starting with an RMSE of about 75% and of about 150% at the first iteration and reaching a value of about 3%. The scatter plot of Figure 14d illustrates a steady decrease of the inflation coefficient α_k suggesting a reduction on the error function value iteration by iteration (Equation 5).

The comparison between the RMSE error obtained with ensemble smoother (ES)-multiple data assimilation (MDA)-restricted step (RS) and ES-MDA (Figure 15a,b), evaluated maintaining the same prior information, shows that the adaptive algorithm guarantees lower RMSE values. This effect is particularly evident in Figure 15b, where the red line (ES-MDA), associated with ρ_{a1}, reaches an RMSE of almost 10%. From Figures 14c and 15, we can affirm that at each assimilation step, the entire ensemble of predicted data tend to fit the observed data.

This is evident if we compare the ensemble of predicted data at the first and at the last iteration (Figure 16). In particular, Figure 16a–c shows all the data predicted from the ensembles of models P^{prior} and Λ^{prior} (in orange), which are not able to predict the observed data (in red). During the inversion run, the entire ensembles constantly decrease the prediction error, until all the ensembles are able to well predict the observed data (Figure 16b–d). Indeed, as the ensembles P^{prior} and Λ^{prior} are randomly drawn from the prior distributions, the corresponding RMSEs are large (from about 20% to more than 100%, Figure 17a,b). On the contrary, after the last iteration, the ensembles P^{post} and Λ^{post} are able to predict the observed data with low prediction error (about 3% in Figure 17c, around 4%–5% in Figure 17d). At this stage, we compute the posterior mean models and the associated uncertainties (Figure 18). As expected from previous knowledge of the study area, the mean model ρ_0 exhibits a shallow high resistivity layer that decreases its thickness from left to right and can be interpreted as the fill cover zone. Below that high resistivity zone, it is evident a low resistivity region at an
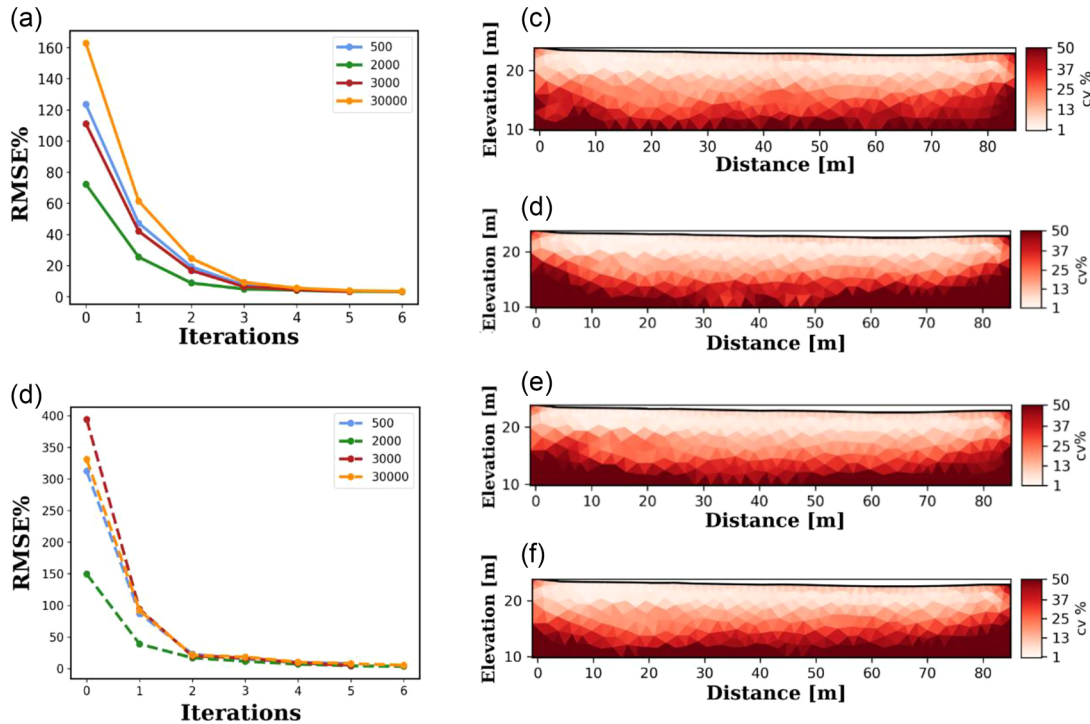
FIGURE 12 (a) Prediction error of the data ρ_{a0} as the P^{prior} ensemble size varies. A total of 500, 2000, 3000 and 30,000 models in light blue, green and red, respectively. (b) Prediction error of the data ρ_{a1} as the Λ^{prior} ensemble size varies. A total of 500, 2000, 3000 and 30,000 models in light blue, green and red, respectively. (c) Coefficients of variation considering 500 models. (d) Coefficients of variation considering 2000 models. (e) Coefficients of variation considering 3000 models. (f) Coefficients of variation considering 30,000 models.

elevation between 20 and 15 m, whereas below 15 m, the model shows a large lateral resistivity variation. The low-resistivity zone is interpreted as the unconfined sandy aquifer that we can find at that depth (Høyer et al., 2019), which might be discontinuous due lateral to variation in grain sizes. The deep portion of the model might be associated with moraine clay; however, the resistivity values manifest some lateral discontinuities that need to be investigated in more detail. To better interpret the results, we compute the standard deviation from the final ensemble of posterior realizations (Figure 18b).

It seems to suggest that the high uncertainty values are associated with the deepest cells and shallow high resistivity values. To avoid uncertainties misinterpretation, we compute the coefficient of variation (cv) (Figure 18c), which eases the comparison between uncertainty values especially when the resistivity range is wide. Specifically, we observe low ambiguity in the shallow part of the model, an increase of cv values in depth and laterally due to the poor data illumination. In other words, being the sensitivity poor, in that portion of the model, a large range of resistivity values give rise to similar data fitting.

This is confirmed by Figure 19 which shows examples of six posterior realizations drawn from the ensemble P^{post}. We observe that all the models univocally predict the resistivity anomalies from the surface down to 16 m of elevation, whereas the variability of the reconstructed resistivity values

increases at the lateral and bottom edge of the investigated area (see Figure 19).

The estimated resistivity changes between ρ_0 and ρ_1 are shown in Figure 20a. The figure shows the presence of three anomalies characterized by high value of λ_ρ (about 2.5) at the elevation between 20 and 16 m. This means that from t_0 to t_1, that is from the first and second acquisition, the resistivity has more than doubled in that portion of the models. We interpret the anomalies as a decrease in saturation of the sandy aquifer, which is discontinuous probably due to the lateral change in grain size (Høyer et al., 2019). Below those central high variation anomalies, we note a decrease of resistivity corresponding to λ_ρ values of about 0.5. Analysing the standard deviation map of Figure 20b, computed from the posterior marginal probability density functions of each cell, we note a correlation between high uncertainties and high resistivity values. Thus, to better evaluate and compare the estimated uncertainty, we calculate the cv (Figure 20c). It is clear that the ambiguous portions of the model are located at the bottom and at the lateral side of the model where the data illumination is poor. On the contrary, low uncertainties are located at the shallowest part of the model and above an elevation of 15 m where the three high ratio anomalies are present. In conclusion, the coefficient of variation in Figure 20c suggests that the three high ratio anomalies are reliable.
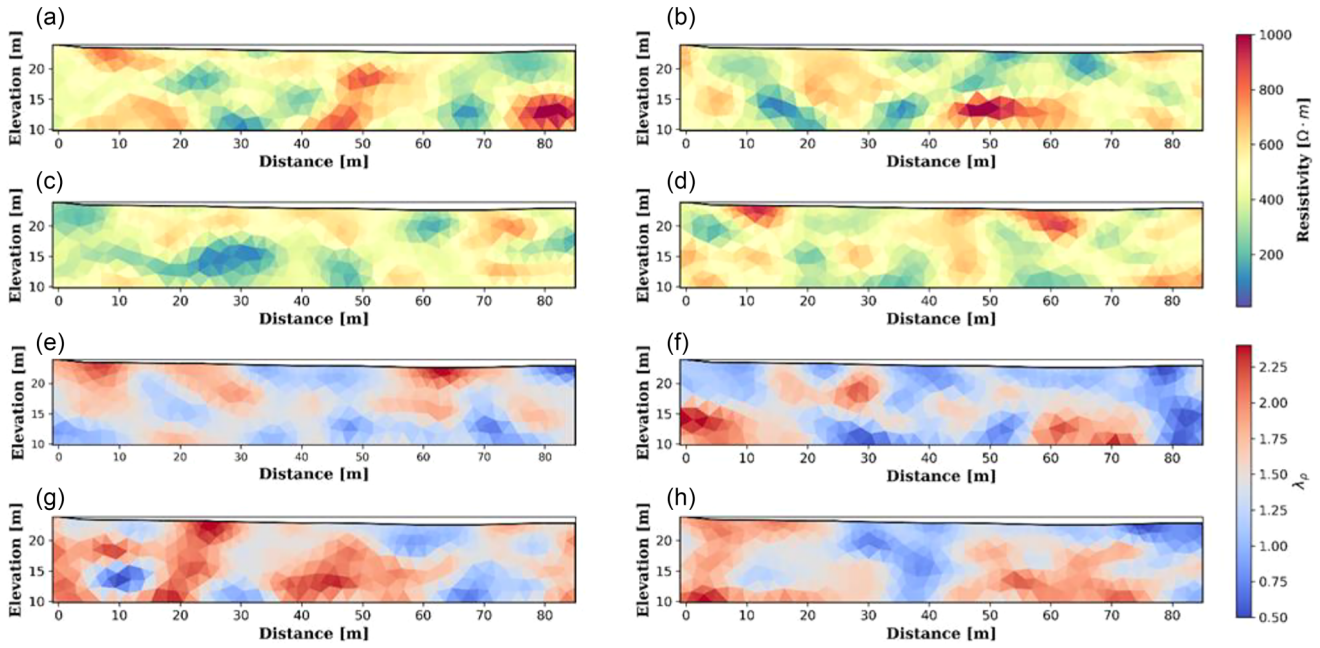
FIGURE 13 (a–d) Prior realizations drawn from the prior ensemble P^{prior}. (e–h) Prior realizations drawn from the ensemble Λ^{prior}.
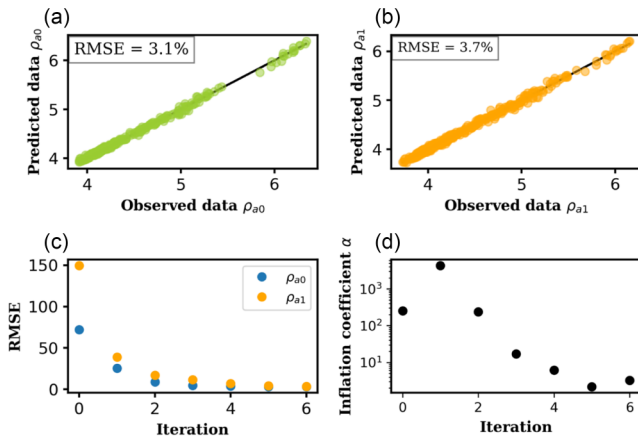

FIGURE 14 Data misfit and cross plot between observed and predicted data ρ_{a0}. (b) Data misfit and cross plot between observed and predicted data ρ_{a1} (c) root mean square error (RMSE) evolution during the iterations. (d) Inflation coefficient trend.

FIGURE 15 (a) Root mean square error (RMSE) error of ρ_{a0} prediction obtained from ensemble smoother (ES)-multiple data assimilation (MDA) and ES-MDA-restricted step (RS). (b) RMSE of ρ_{a1} prediction obtained from ES-MDA and ED-MDA-RS.

As a confirmation of this, analysing the posterior realizations extracted from the ensemble Λ^{post}(Figure 21), we observe that each realization exhibits the same anomalies up to an elevation of 15 m, whereas below that elevation the variability between each model is large. To validate our results, we employ the cascaded inversion algorithm, a more traditional gradient-based inversion approach that in inverts the two datasets separately, but exploiting the model estimated from the dataset ρ_{a0} as the starting model for the inversion of ρ_{a1}(Miller et al., 2008). For this purpose, we exploit the BERT

open-source software package. Figure 22 shows the models estimated by of the ES-MDA-RS algorithm and by the cascaded inversion. As expected, the cascaded inversion is faster than our algorithm; indeed, the computational time is less than 1 min. However, it is clear the similarity between the ρ_0 estimated by the two algorithms (Figure 22a–d) especially above an elevation of 15 m. In addition, even though the results of the gradient based inversion seem to be smoother than the stochastic ones, the locations of the anomaly are consistent. The resistivity variations (Figure 22b–e) are completely
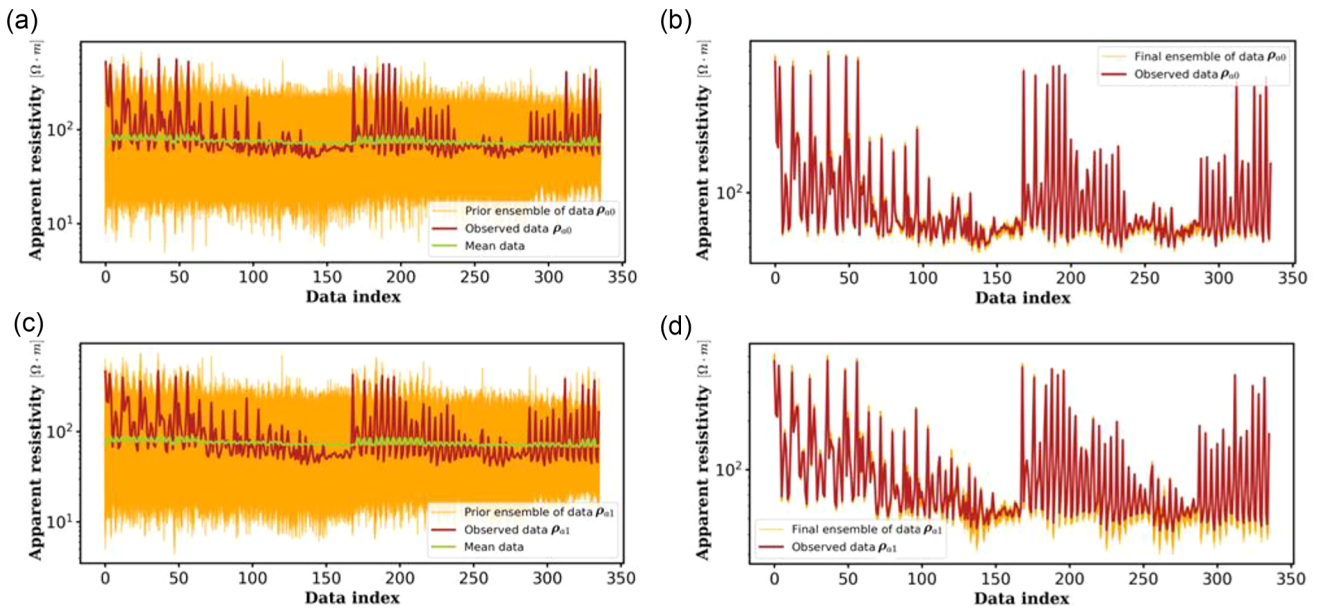
FIGURE 16 (a) Ensemble of 2000 predicted data from the ensemble P^{prior} (orange) and the observed data ρ_{a0} (red). (b) Comparison between the data predicted b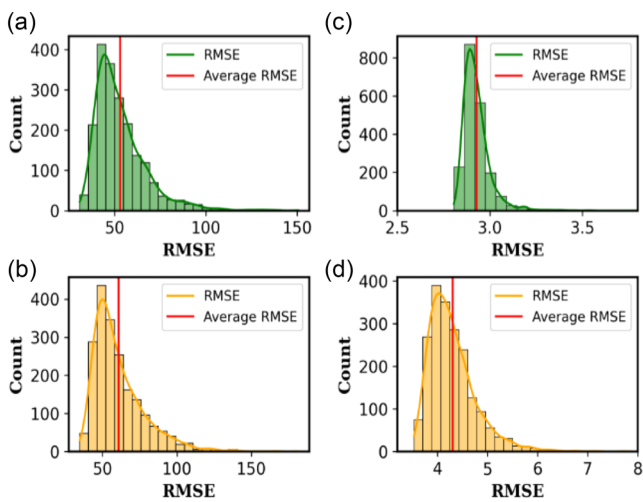y the ensemble P^{post} (orange) and the observed data ρ_{a0} (red). (c) Ensemble of 2000 predicted data; from the Λ^{prior} (orange) and the observed data ρ_{a1} (red). (d) Comparison between the ensemble of data predicted by the ensemble Λ^{post} (green orange) and the observed data (red).

FIGURE 17 (a) Histogram of the prediction root mean square error (RMSE) obtained from the ensemble P^{prior}. (B) Histogram of the prediction RMSE obtained from the prior ensemble Λ^{prior}. (c) Histogram of the prediction RMSE associated with the ensemble P^{post}. (d) Histogram of the prediction RMSE associated with the ensemble Λ^{post}.

FIGURE 18 (a) Predicted mean model ρ_0 by the ensemble smoother (ES)-multiple data assimilation (MDA)-restricted step (RS) algorithm. (b) Standard deviation map computed from the marginal posterior distributions. (c) Coefficient of variation associated with the mean model ρ_0.

coherent in terms of location and magnitude, especially the resistivity increase that we already interpreted. Moreover, the resistivity estimated at the time t_1 in Figure 22c,f exhibits the same anomalies distribution in the whole model where illumination is not poor. This comparison suggests the reliability of the ES-MDA-RS for time-lapse ERT inversion purposes.
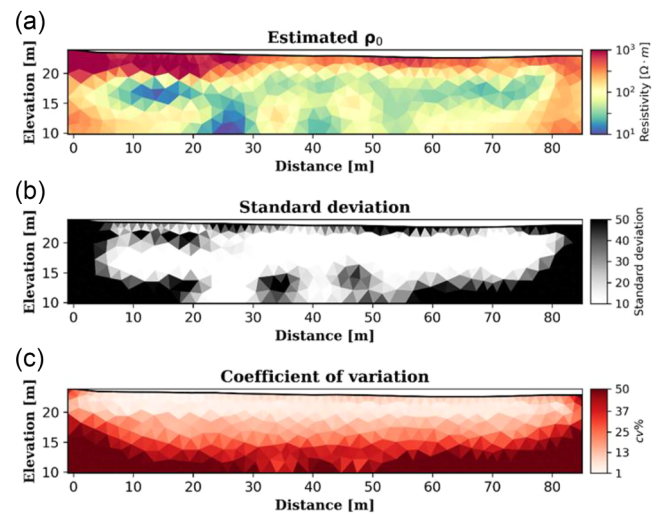
CONCLUSION

In this paper, we formulate the time-lapse (TL) electrical resistivity tomography (ERT) data inversion as a data-assimilation problem to quantify the uncertainties of the inverse solution. The implemented ensemble smoother
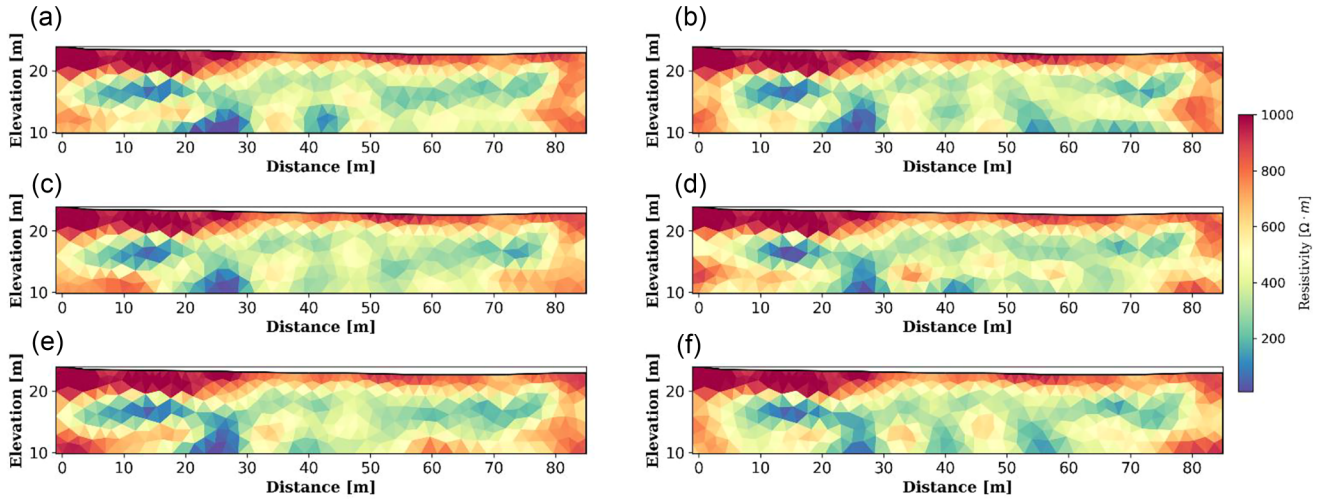
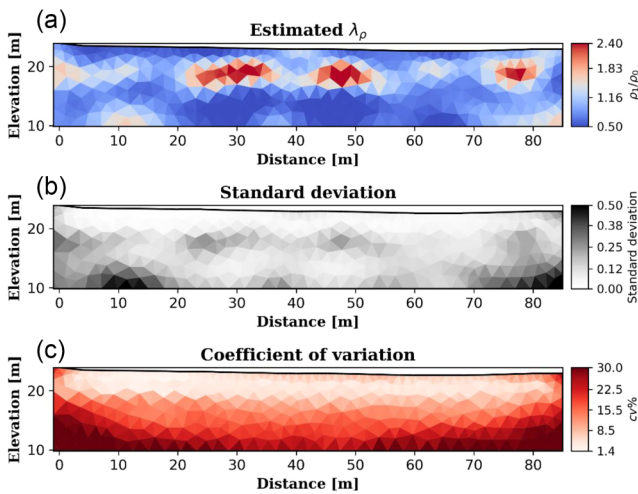**FIGURE 19**   (a–f) Realizations drawn from the ensemble P^{post}.

FIGURE 20   (a) Predicted mean ensemble model $\boldsymbol{\lambda}_\rho$ by the ensemble smoother (ES)-multiple data assimilation (MDA)-restricted step (RS) algorithm. (b) Standard deviation map computed from marginal posterior distributions. (c) Coefficient of variation associated with the mean model $\boldsymbol{\lambda}_\rho$.

(ES)-multiple data assimilation (MDA)-restricted step (RS) casts the problem in a Bayesian setting, allowing for the integration of prior knowledge about the expected changes in resistivity to recover the posterior probability density function. We compute the moments of the prior distributions from the observed data without any other constraints to test the applicability of the algorithm. Despite this, the ES-MDA-RS is able to estimates the resistivity model, the resistivity changes and the uncertainties.

The inversion of the synthetic TL data validates the effectiveness of the approach, resulting in a satisfactory estimation of the resistivity variation both in the shallow and deep part of the model. Moreover, the integrated interpretation of the standard deviation and the coefficients of variation guarantee the robust interpretation of the anomalies, distinguishing the more reliable portions of the model from those affected by poor sensitivity or artefacts.

The TL ES-MDA-RS applied to the Pillemark landfill monitoring station is able to map the resistivity variation of the unconfined aquifer with a good spatial resolution and low root mean square error. In particular, the clear change in resistivity that we interpret as the decrease of the saturation of the aquifer corresponds with low uncertainty. Thus, the uncertainty estimation carried out using both the standard deviation and the coefficient of variation provides a valuable tool to assess the reliability of the mapped anomalies and the portions of the models affected by poor sensitivity. The comparable model estimation obtained through the deterministic cascade inversion validates the ES-MDA-RS results.

Even though the assumptions required by the approach limit the applicability to Gaussian prior distribution and Gaussian error on the data, the main advantage of the proposed algorithm is the appraisal of the uncertainty associated with resistivity variation through a computationally feasible stochastic approach. The automatic selection of the inflation coefficient and the stopping criteria simplify the preliminary setting phase of the ES-MDA algorithm. In our example, the adaptive choice of the inflation coefficient helps the inversion obtain a lower error prediction. This paper demonstrates
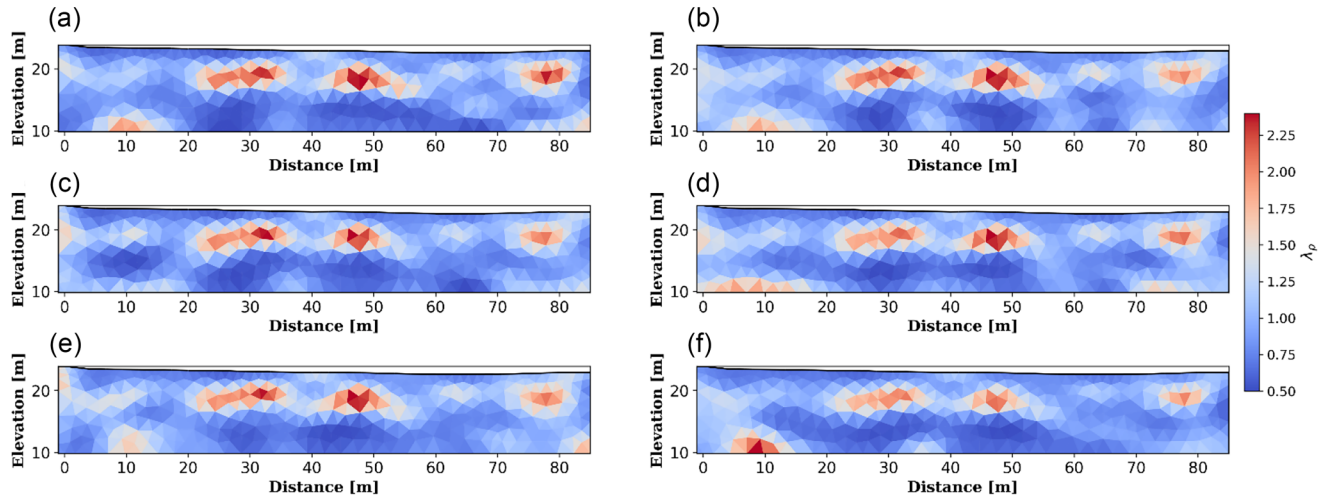
FIGURE 21   (a–f) Realizations drawn from the posterior ensemble Λ^{post}.
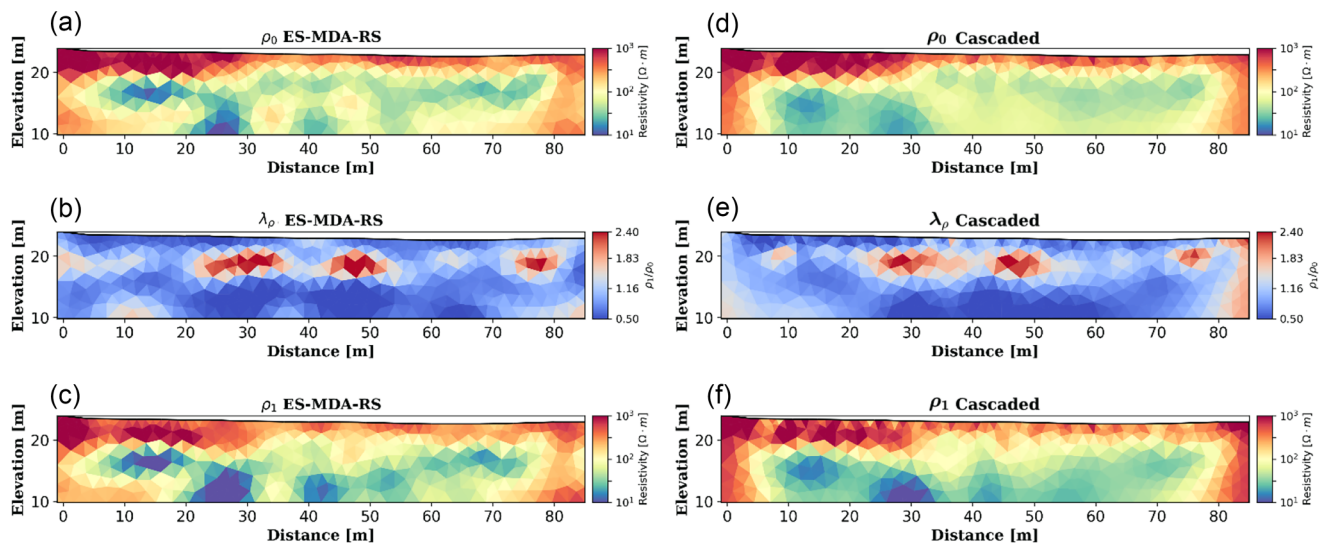

FIGURE 22   (a–c) Estimated models by ensemble smoother (ES)-multiple data assimilation (MDA)-restricted step (RS). (d–f) Estimated models by the cascade inversion algorithm.

the potential of data assimilation to solve the non-linear ERT problem in the TL framework, making it a valid alternative for inverting permanent monitoring station data.

DATA AVAILABILITY STATEMENT

The data that support the findings of this study are available from the corresponding author upon reasonable request.

ORCID

Alessandro Vinciguerra https://orcid.org/0000-0003-3452-1579
Mattia Aleardi https://orcid.org/0000-0003-1433-0281

REFERENCES

Aleardi, M., Vinciguerra, A. & Hojat, A. (2021a) A convolutional neural network approach to electrical resistivity tomography. *Journal of Applied Geophysics*, 193, 104434. https://doi.org/10.1016/j.jappgeo.2021.104434

Aleardi, M., Vinciguerra, A. & Hojat, A. (2021b) Ensemble-based electrical resistivity tomography with data and model space compression. *Pure and Applied Geophysics*, 178, 1781–1803. https://doi.org/10.1007/s00024-021-02730-1

Arosio, D., Munda, S., Tresoldi, G., Papini, M., Longoni, L. & Zanzi, L. (2017) A customized resistivity system for monitoring saturation and seepage in earthen levees: installation and validation. *Open Geosciences*, 9(1), 457–467. https://doi.org/10.1515/geo-2017-0035

Audebert, M., Clément, R., Grossin-Debattista, J., Günther, T., Touze-Foltz, N. & Moreau, S. (2014) Influence of the geomembrane on time-lapse ERT measurements for leachate injection monitoring. *Waste Management*, 34(4), 780–790. https://doi.org/10.1016/j.wasman.2014.01.011

Auken, E., Christiansen, A.V., Jacobsen, B.H. & Foged, N. (2005) Piecewise 1D laterally constrained inversion of resistivity data. *Geophysical Prospecting*, 53, 497–506. https://doi.org/10.1111/j.1365-2478.2005.00486.x

Bording, T.S., Fiandaca, G., Auken, E. & Christiansen, A.V. (2018) Monitoring seasonal variation of leaching from a landfill through time-domain induced polarization. In: 5th International *Workshop on Induced Polarization, Rutgers University in Newark, NJ, 3–5 October 2018*. Ontario, University of Waterloo.

Batista-Rodríguez, J.A. & Pérez-Flores, M.A. (2021) Contribution of ERT on the study of Ag–Pb–Zn, fluorite, and barite deposits in northeast Mexico. *Minerals*, 11, 249. Available from: https://doi.org/10.3390/min11030249

Chambers, J.E., Meldrum, P.I., Gunn, D.A., Wilkinson, P.B., Kuras, O., Weller, A.L. et al.(2009) Hydrogeophysical monitoring of landslide processes using automated time-lapse electrical resistivity tomography (ALERT). In: 15th European *Meeting of Environmental and Engineering Geophysics*. Utrecht, European Association of Geoscientists & Engineers.https://doi.org/10.3997/2214-4609.20147066

Chen, Y. & Oliver, D. (2013) Levenberg-Marquardt forms of the iterative ensemble smoother for efficient history matching and uncertainty quantification. *Computer Geoscience*, 17, 689–703. Available from: https://doi.org/10.1007/s10596-013-9351-5

Clément, R., Oxarango, L., & Descloitres, M. (2011) Contribution of 3-D time-lapse ERT to the study of leachate recirculation in a landfill. *Waste Management*, 31(3), 457–467. Available from: https://doi.org/10.1016/j.wasman.2010.09.005

Crawford, M.M., Bryson, L.S., Woolery, E.W. & Wang, Z. (2018) Using 2-D electrical resistivity imaging for joint geophysical and geotechnical characterization of shallow landslides. *Journal of Applied Geophysics*, 157, 37–46. Available from: https://doi.org/10.1016/j.jappgeo.2018.06.009

Emerick, A.A. (2019). Analysis of geometric selection of the data-error covariance inflation for ES-MDA. *Journal of Petroleum Science and Engineering*, 182, 106168. https://doi.org/10.1016/j.petrol.2019.06.032

Emerick, A. & Reynolds, A. (2013) Ensemble smoother with multiple data assimilation. *Computers and Geosciences*, 55, 3–15. Available from:https://doi.org/10.1016/j.cageo.2012.03.011

Evensen, G. (1994) Sequential data assimilation with a non-linear quasi geostrophic model using Monte Carlo methods to forecast error statistics. *Journal of Geophysical Research*, 99, 10143–10162. Available from: https://doi.org/10.1029/94JC00572

Evensen, G., Vossepoel, F.C. & van Leeuwen, P.J. (2022) *Data assimilation fundamentals*. Berlin: Springer.

Everitt, B.S. (1998) *Cambridge dictionary of statistics*. Cambridge: Cambridge University Press.

Fernández-Martínez, J.L., Fernández-Muñiz, L., Pallero, J.L.G. & Pedruelo-González, L.M. (2013) From Bayes to Tarantola: new insights to understand uncertainty in inverse problems. *Journal of Applied Geophysics*, 98, 62–72. Available from:https://doi.org/10.1016/j.jappgeo.2013.07.005

Fiandaca, G., Doetsch, J., Vignoli, G. & Auken, E. (2015) Generalized focusing of time-lapse changes with applications of direct current and time-domain induced polarization inversions. *Geophysical Journal International*, 203, 1101–1112. Available from: https://doi.org/10.1093/gji/ggv350

Gaël, D., Tanguy, R., Nicolas, M. & Frédéric, N. (2017) Assessment of multiple geophysical techniques for the characterization of municipal waste deposit sites. *Journal of Applied Geophysics*, 145, 74–83. Available from: http://doi.org/10.1016/J.JAPPGEO.2017.07.013

Gao, G. & Reynolds, A.C. (2006) An improved implementation of the LBFGS algorithm for automatic history matching. *SPE Journal*, 11(01), 5–17. Available from: https://doi.org/10.2118/90058-PA

Grana, D., Passos de Figueiredo, L. & Azevedo, L. (2019) Uncertainty quantification in Bayesian inverse problems with model and data dimension reduction. *Geophysics*, 84(6), M15–M24. Available from: http://doi.org/10.1190/geo2019-0222.1

Gunn, D.A., Chambers, J.E., Dashwood, B.E., Lacinska, A., Dijkstra, T. & Uhlemann, S. et al. (2018) Deterioration model and condition monitoring of aged railway embankment using non-invasive geophysics. *Construction and Building Materials*, 170, 668–678. Available from: http://doi.org/10.1016/j.conbuildmat.2018.03.066

Gunther, T. & Rucker, C. (2012) Boundless electrical resistivity tomography (BERT) v. 2.0 – open access software for advanced and flexible imaging. *Schlumberger Symposium – 100 years of electrical imaging, Paris*

Hayley, K., Pidlisecky, A., & Bentley, L.R. (2011). Simultaneous time-lapse electrical resistivity inversion. *Journal of Applied Geophysics*, 75(2), 401–411. https://doi.org/10.1016/j.jappgeo.2011.06.035

Hilbich, C., Fuss, C. & Hauck, C. (2011), Automated time-lapse ERT for improved process analysis and monitoring of frozen ground. *Permafrost and Periglacial Processes*, 22, 306–319. Available from: https://doi.org/10.1002/ppp.732

Hojat, A., Arosio, D., Ivanov, V.I., Longoni, L., Papini, M., Scaioni, M. et al. (2019) Geoelectrical characterization and monitoring of slopes on a rainfall-triggered landslide simulator. *Journal of Applied Geophysics*, 170, 103844. Available from: https://doi.org/10.1016/j.jappgeo.2019.103844

Høyer, A.S., Klint, K.E.S., Fiandaca, G., Maurya, P.K., Christiansen, A.V. & Balbarini, N. et al. (2019) Development of a high-resolution 3D geological model for landfill leachate risk assessment. *Engineering Geology*, 249, 45–59. Available from:https://doi.org/10.1016/j.enggeo.2018.12.015

Kim, J.-H., Supper, R., Tsourlos, P., & Yi, M.-J. (2013). Four-dimensional inversion of resistivity monitoring data through Lp norm minimizations. *Geophysical Journal International*, 195(3), 1640–1656. https://doi.org/10.1093/gji/ggt324

Kim, J.-H., Yi, M.-J., Park, S.-G. & Kim, J. (2009) 4D inversion of DC resistivity monitoring data acquired over a dynamically changing earth model. *Journal of Applied Geophysics*, 68, 522–532. Available from: https://doi.org/10.1016/j.jappgeo.2009.03.002

Labreque, D. & Yang, X. (2001) Difference inversion of ERT data: a fast inversion method for 3-D in situ monitoring. *Journal of Environmental Engineering Geophysics*, 6, 83–89. Available from: https://doi.org/10.4133/JEEG6.2.83

Le, D.H., Emerick, A.A. & Reynolds, A.C. (2016) An adaptive ensemble smoother with multiple data assimilation for assisted history match-

ing. *SPE Journal*, 21, 2195–2207. Available from: https://doi.org/10.2118/173214-PA

Li, R., Reynolds, A.C. & Oliver, D.S. (2003) History matching of three-phase flow production data. *SPE Journal*, 8(04), 328–340. Available from: https://doi.org/10.2118/87336-PA

Liu, Q., Beller, S., Lei, W., Peter, D., & Tromp, J. (2021). Pre-conditioned BFGS-based uncertainty quantification in elastic full-waveform inversion. *Geophysical Journal International*, 228(2), 796–815. https://doi.org/10.1093/gji/ggab375

Liu, M. & Grana, D. (2018) Ensemble-based joint inversion of PP and PS seismic data using full Zoeppritz equations. In: *SEG technical program expanded abstracts*. Houston, Society of Exploration Geophysicists. pp. 511–515. Available from:https://doi.org/10.1190/segam2018-2993625.1

Liu, S., (2012) Confidence interval estimation for coefficient of variation Thesis. Georgia State University. Available from: https://doi.org/10.57709/2785351

Miller, C.R., Routh, P.S., Brosten, T.R. & McNamara, J.P. (2008) Application of time-lapse ERT imaging to watershed characterization. *Geophysics*, 73(3), G7–G17. Available from: https://doi.org/10.1190/1.2907156

Mosegaard, K. & Tarantola, A. (1995) Monte Carlo sampling of solutions to inverse problems. *Journal of Geophysical Research*, 1001, 12431–12448. Available from: https://doi.org/10.1029/94JB03097

Oliver, D.S., Reynolds, A.C., & Liu, N. (2008). Inverse Theory for Petroleum Reservoir Characterization and History Matching. https://doi.org/10.1017/cbo9780511535642

Ramirez, A.L., Nitao, J.J., Hanley, W.G., Aines, R., Glaser, R.E., Sengupta, S.K. et al. (2005) Stochastic inversion of electrical resistivity changes using a Markov Chain Monte Carlo approach. *Journal of Geophysical Research: Solid Earth*, 110(2), 1–18, Available from: https://doi.org/10.1029/2004JB003449

Reynolds, A.C., Zafari, M. & Li, G. (2006) *Iterative forms of the ensemble Kalman filter*. Moscow: European Association of Geoscientists and Engineers. Available from: https://doi.org/10.3997/2214-4609.201402496

Rubio-Melendi, D., Gonzalez-Quirós, A., Roberts, D., García, M.C.F., Domínguez, A.C., Pringle, J.K. et al. (2018) GPR and ERT detection and characterization of a mass burial, Spanish Civil War, northern Spain. *Forensic Science International*, 287, e1–e9. Available from: https://doi.org/10.1016/j.forsciint.2018.03.034

Tarantola, A. (2005) *Inverse problem theory and methods for model parameter estimation*. Philadelphia, PA: Society for Industrial and Applied Mathematics.

Tresoldi, G., Arosio, D., Hojat, A., Longoni, L., Papini, M. & Zanzi, L. (2019) Long-term hydrogeophysical monitoring of the internal conditions of river levees. *Engineering Geology*, 259, 105139. Available from: https://doi.org/10.1016/j.enggeo.2019.05.016

Tso, C.-H.M., Kuras, O., Wilkinson, P.B., Uhlemann, S., Chambers, J.E., Meldrum, P.I. et al. (2017) Improved characterisation and modelling of measurement errors in electrical resistivity tomography (ERT) surveys. *Journal of Applied Geophysics*, 146, 103–119. Available from: https://doi.org/10.1016/j.jappgeo.2017.09.009

Vinciguerra, A., Aleardi, M., Hojat, A., Loke, M.H. & Stucchi, E. (2021) Discrete cosine transform for parameter space reduction in Bayesian electrical resistivity tomography. *Geophysical Prospecting*, 70(1), 193–209. Available from: https://doi.org/10.1111/1365-2478.13148

Whiteley, J., Chambers, J.E. & Uhlemann, S. (2017) Integrated monitoring of an active landslide in Lias Group Mudrocks, North Yorkshire, UK. In: Hoyer, S. (Ed.) *GELMON 2017: 4th International Workshop on Geoelectrical Monitoring: Book of a*bstracts. Orléans, France, IRIS Instruments. p. 27.